

Performance and Durability of Membrane Electrode Assemblies Using Ni-Based OER Catalysts for Anion Exchange Membrane Water Electrolysis

Soichiro Natori, Sayaka Takahashi, Toshio Iwataki, Takayuki Asakawa, Guoyu Shi, Katsuyoshi Kakinuma, Kenji Miyatake, and Makoto Uchida*



Cite This: ACS Appl. Energy Mater. 2025, 8, 5823–5834



Read Online

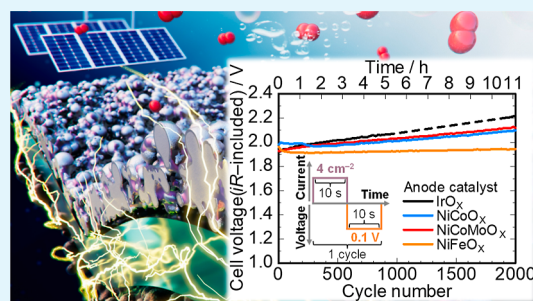
ACCESS |

Metrics & More

Article Recommendations

Supporting Information

ABSTRACT: For the large-scale commercialization of anion exchange membrane water electrolysis (AEMWE), it is essential to develop electrocatalysts that exhibit both high activity and durability. Here, we investigate the performance of membrane-electrode assemblies (MEAs) up to a current density of 4 A cm^{-2} , as well as durability assessments, including startup ($4 \text{ A cm}^{-2}, 10 \text{ s}$) and shutdown ($0.1 \text{ V}, 10 \text{ s}$) cycles and constant current density (1 A cm^{-2}) and load fluctuations ($0\text{--}2 \text{ A cm}^{-2}$) cycles at 80°C , of AEMWE single cells using several in-house developed Ni-based oxide catalysts (NiCoO_x , NiCoMoO_x , NiFeO_x) for the anode, and the in-house developed anion exchange ionomer (QPAF-4) for both the membrane and the catalyst layer binder. The results of the 2000-cycle accelerated degradation test demonstrate the extremely high stability of NiFeO_x , together with high MEA performance, $1.94 \text{ V}@4 \text{ A cm}^{-2}$, achieved after the durability test. Based on these results, we provide strategies for the development of electrocatalysts achieving high performance and durability on the MEA level.



KEYWORDS: anion exchange membrane water electrolysis, membrane electrode assemble, electrocatalyst, durability, start–stop operation

1. INTRODUCTION

For a carbon-neutral society, hydrogen is expected to be an ideal energy carrier.^{1–4} Water electrolysis is a promising technology for producing green hydrogen from intermittent renewable energy sources such as solar and wind power.^{2,5–10} Anion exchange membrane water electrolysis (AEMWE) has been attracting attention because of the availability of nonprecious metal catalysts.^{11–13} However, there are still several bottlenecks in AEMWE that must be overcome for large-scale commercialization, such as low operating current densities and low durability compared to proton exchange membrane water electrolysis (PEMWE).^{14,15} For the large-scale commercialization of AEMWE, it is extremely important to enhance both the activity and stability of the hydrogen evolution reaction (HER) and oxygen evolution reaction (OER) catalysts.¹⁴ In particular, since OER is a complex four-electron transfer process and the reaction is significantly slower than the HER, the development of highly active and robust OER catalysts is essential.^{2,11,14} In recent years, transition metal (Ni, Fe, Co)-based catalysts have attracted a great deal of attention because they exhibit excellent OER activity in alkaline media, and their effectiveness has been widely demonstrated.^{2,10,14,16–18} For example, Lee et al. systematically investigated Fe–Co–Ni ternary amorphous electrocatalysts and achieved membrane-electrode assemble (MEA) perform-

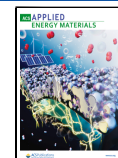
ance of 2.0 A cm^{-2} @ 1.89 V at 60°C and 1.0 M KOH by optimizing the composition.¹⁷ In addition, Yang et al. developed multiple-layered ternary NiFeM (M: Co, Mn, or Cu) nanofoam OER catalysts by incorporating the third metals (Cu, Mn, and Co) into the conventional NiFe catalyst and controlling the electronic structure and morphology.¹⁸ Among these, the NiFeMn catalyst delivered a remarkable MEA performance of 2.0 A cm^{-2} @ 1.7 V at 80°C , superior to the IrO_2 reference when 0.1 M KOH solution was supplied to the anode.¹⁸ Regarding these reports on Ni-based OER catalysts, the durability of the MEA was also investigated, but all of them were limited to the durability evaluation at a relatively low current density of 0.5 A cm^{-2} .^{17,18} In our research group, NiCoO_x , NiFeO_x , and NiCoMoO_x catalysts with an amorphous oxide layer on the surface of a crystalline alloy core have been developed based on the flame synthesis method.^{19–21} These catalysts exhibit higher OER activity than commercial IrO_x and most reported OER catalysts, with the

Received: January 27, 2025

Revised: April 8, 2025

Accepted: April 21, 2025

Published: April 28, 2025



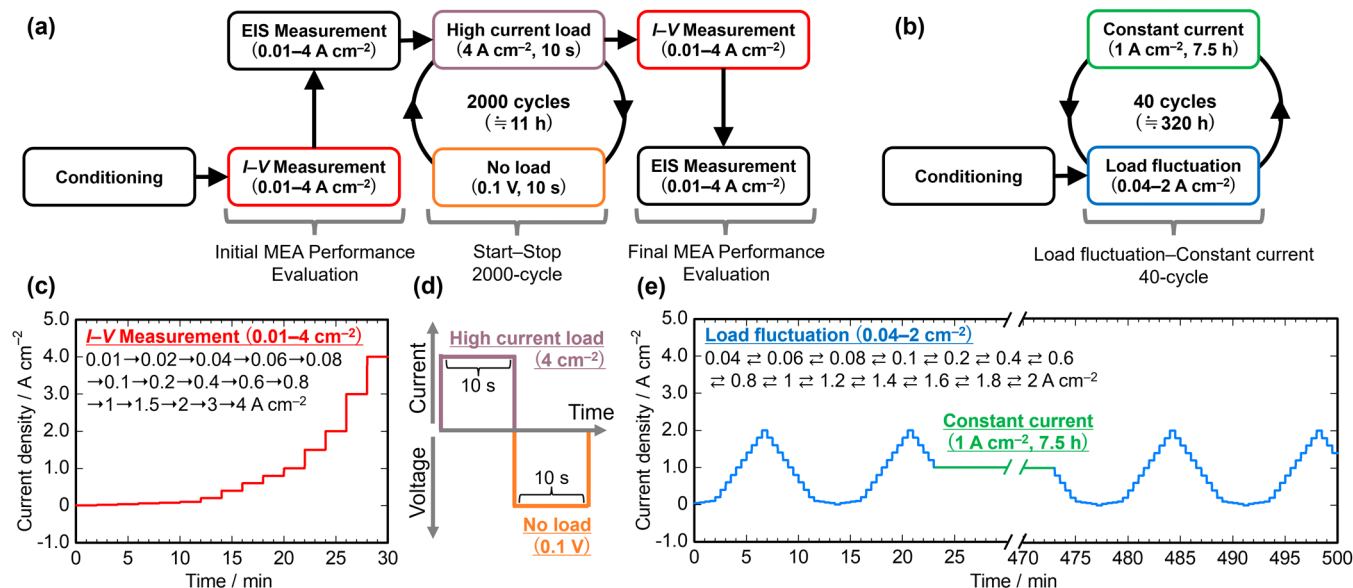


Figure 1. (a) A series of evaluation protocols for cell conditioning and subsequent evaluation of initial MEA performance, start (4 A cm^{-2} , 10 s)—stop (0.1 V, 10 s) 2000-cycle accelerated degradation test, and final MEA performance, and (b) a load fluctuation ($0.04\text{--}2 \text{ A cm}^{-2}$)—constant (1 A cm^{-2} , 7.5 h) current 40-cycle durability test. A detailed time course of the applied current density in (c) $I\text{-}V$ measurement, and (e) load fluctuation-constant current durability test; and (d) detailed time course of the current and voltage control in the ADT. All measurements were taken with a 1 M KOH aqueous solution supplied to both sides of the cell at 10 mL min^{-1} at 80°C .

alloy core and surface oxide playing the roles of high electronic conductivity and OER active sites, respectively.²¹ In addition, since all of the catalyst particles are interconnected to form a network structure, it is expected that the electronic conductive pathway and the efficient release of oxygen gas generated during the OER will be ensured. However, the MEA performance at current densities exceeding 2 A cm^{-2} and the durability during the simulation of the drastic startup and shutdown of renewable energy sources have not been investigated in AEMWE single cells using these OER catalysts for the anode.²¹ When the water electrolyzer is stopped due to the use of renewable electricity, the hydrogen in the cathode gradually crosses over to the anode side, so the anode potential may eventually drop to around 0 V vs RHE, and this tendency is even more pronounced in pressurized operation.²² Therefore, repeated startup and shutdown cycles cause the anode catalyst to undergo redox cycles, accelerating catalyst degradation.²² In order to simulate this situation, Mitsubishi et al., have proposed a mixed cycle test of current control (4 A cm^{-2}) and potential control (0.1 V) as a simulated start–stop test for PEMWE.²²

In this study, we sought to propose a design guideline for electrocatalysts combining high performance and durability by carrying out MEA performance evaluations up to a current density of 4 A cm^{-2} , as well as durability evaluations in load ranges that are impossible to perform using a rotating disk electrode (RDE), specifically, startup (4 A cm^{-2} , 10 s) and shutdown (0.1 V, 10 s) cycles and constant current density (1 A cm^{-2}) and load fluctuation ($0.04\text{--}2 \text{ A cm}^{-2}$) cycles, in AEMWE single cells using the Ni-based oxide catalysts.

2. EXPERIMENTAL SECTION

2.1. Characterization of Catalysts. The morphologies of the in-house developed NiCoO_x , NiCoMoO_x , and NiFeO_x catalysts were observed with transmission electron microscopy (TEM, for Figure S1) (H9500, Hitachi High-Tech Corporation, Japan).^{19–21} The specific surface areas of the NiCoO_x , NiCoMoO_x , NiFeO_x catalysts

and the commercial IrO_x catalyst (SA100, ELC-1510, TANAKA PRECIOUS METAL TECHNOLOGIES Co., Ltd., Japan) were estimated by the Brunauer–Emmett–Teller (BET) adsorption method (Autosorb-iQ, Anton Paar GmbH, Austria).^{19–21} The electronic conductivities were evaluated by using a DC two-probe conductivity measurement system (Panasonic Corporation, Japan) with the catalyst powder compressed at approximately 12 MPa.

2.2. Preparation of MEAs. The anode catalyst ink was prepared using the NiCoO_x , NiCoMoO_x , NiFeO_x , and IrO_x catalysts, ultrapure water, and methanol by zirconia ball milling for 30 min.^{19–21} A 1 wt % solution of QPAF-4 binder (IEC = 1.5 mequiv g⁻¹) in methanol was added to the resultant slurry followed by ball milling for another 30 min.²³ The mass ratio of QPAF-4 binder to the anode catalyst was adjusted to 0.15. This catalyst ink was sprayed onto one side of a QFAF-4 membrane (IEC = 1.5 mequiv g⁻¹, 50 μm thick) by using a pulse-swirl-spray (PSS, Nordson Corporation, USA) technique to prepare an anode catalyst-coated-membrane (CCM). The synthetic procedure of the QPAF-4 copolymers is shown in Scheme S1.²³ The cathode catalyst ink was prepared using a commercial Pt/C catalyst (TEC10E50E, TANAKA PRECIOUS METAL TECHNOLOGIES Co., Ltd., Japan), ultrapure water, and methanol by zirconia ball milling for 30 min. To this slurry, a 1 wt % solution of QPAF-4 binder (IEC = 2.0 mequiv g⁻¹) in methanol was added and ball milled for another 30 min. The mass ratio of the binder to the carbon support was 0.6. This catalyst ink was sprayed onto the back side of anode CCM. The CCM was dried at 60°C overnight and hot pressed at 80°C and 14.6 kgf cm^{-2} for 3 min. The electrode area was 1 cm^2 , and the amounts of catalyst loaded on the anode (Ni-based catalyst, IrO_x catalyst) and cathode (Pt/CB) side were 2.0 mg cm^{-2} , $1.0 \text{ mg}_{\text{Ir}} \text{ cm}^{-2}$, and $1.0 \text{ mg}_{\text{Pt}} \text{ cm}^{-2}$, respectively. On the anode side, a Ni mesh (1Ni06-020, N.V. Bekaert S.A., Belgium) as a porous transport layer (PTL) and a gasket (EPDM, 200 μm thick) were used. On the cathode side, a carbon paper (TGP H-120, TORAY INDUSTRIES, INC., Japan) and a gasket (EPDM, 300 μm thick) were used. The prepared CCM was mounted in a single cell with Ni separators (straight flow channels) on both the anode and cathode. Gold-plated copper was used as the current collector. A pressure of 7.5 kgf cm^{-2} was applied to seal the single cell.²⁴

2.3. Performance and Durability Evaluation of MEAs. The AEMWE cell performance was evaluated with an electrochemical workstation (Netsuden Ind. Co., Ltd., Japan) combined with a

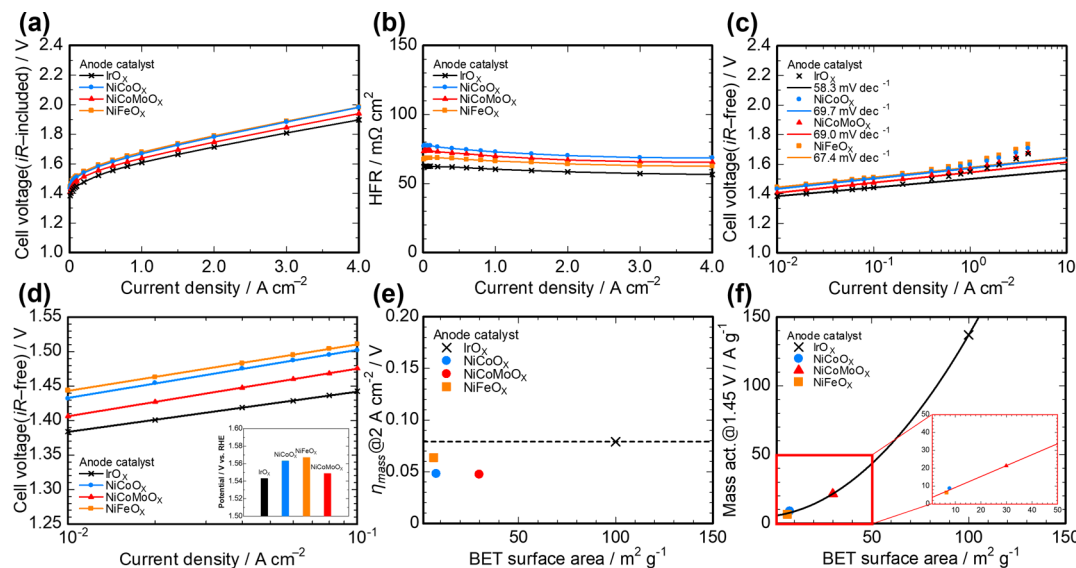


Figure 2. Initial performance of MEAs using various anode catalysts (IrO_x , NiCoO_x , NiCoMoO_x , NiFeO_x) at 80 °C with 1 M KOH solution. (a) Polarization curves, (b) high frequency resistances, (c) iR -free Tafel plots, (d) enlarged view of the Tafel region (the anode potential of each catalyst at 10 mA cm^{-2} measured by RDE, is shown in the inset.^{19–21}), (e) relationship between the deviation from the Tafel slopes at a current density of 2 A cm^{-2} ($\eta_{\text{mass}}@2 \text{ A cm}^{-2}$) and the BET surface area, and (f) the relationship between mass activity at 1.45 V and the BET surface area.

regulated direct current power supply (PWR 401L, Kikusui Electronics Corp., Japan). A 1 M KOH aqueous solution was fed to both sides of the cell at 10 mL min^{-1} at 80 °C. Figure 1a shows a series of evaluation protocols for cell conditioning and subsequent evaluation of initial MEA performance, evaluation of start-stop durability, and final MEA performance. After supplying the electrolyte and stabilizing at 80 °C, the MEA was held at 0.1 A cm^{-2} for 24 h to ensure complete ion exchange. After the completion of the ion exchange, the MEA was activated by sweeping the current density from 0 to 2 A cm^{-2} twice and from 0 to 4 A cm^{-2} twice. The above operations were defined as the conditioning step. After conditioning, I – V measurements and galvanostatic electrochemical impedance measurements were performed as initial MEA performance evaluations using a potentiogalvanostat (VIONIC, Metrohm Autolab B. V., The Netherlands). Figure 1c shows the detailed time course of the applied current density in the I – V measurement. Here, each current density step was held for 2 min from 0.01 to 4 A cm^{-2} , and the average cell voltage for the second minute was used. In the impedance measurement, the high-frequency resistance at each current density was obtained by superimposing an alternating current amplitude under the same current density bias as in the I – V measurement described above. The measurement frequency range was 0.1 MHz to 1 Hz, and the alternating current amplitude was set to 1% of each bias current density (for 0.01–0.1 A cm^{-2} of bias current density range) or 50 mA cm^{-2} (for 0.2–4 A cm^{-2} of bias current density range). Subsequently, we conducted a durability test by repeating 2000 cycles of high current load (4 A cm^{-2}) for 10 and 10 s of stop (0.1 V) following the accelerated degradation test (ADT, Figure 1d) protocol for PEMWE, and recorded the cell voltage changes.²² Here, the reason for using current control instead of potential control during electrolysis is to apply a constant load without being affected by cell resistance. In addition, the constant potential controlled step refers to the situation in which the anode potential drops to near 0 V when hydrogen at the cathode crosses over to the anode during water electrolysis shutdown.²² In addition, a load fluctuation (0.04–2 A cm^{-2}) and constant (1 A cm^{-2} , 7.5 h) current 40-cycle durability test was also conducted (Figure 1b). Here, the detailed time course of the applied current density is shown in Figure 1e. Each current density step in the load fluctuations was held from 0.04 to 2 A cm^{-2} for 30 s. The generated hydrogen and oxygen flow rates were measured by mass flowmeters (8500 MM, KOFLOC Corp., Japan) and the Faradaic efficiency was calculated by dividing the gas generation rate per hour by the theoretical generation rate.

2.4. Characterization of Catalyst Layers. In order to observe the changes in the cross-section of the catalyst layer before and after the durability test, the MEA was carefully disassembled from the cell and washed with ultrapure water. Subsequently, the PTLs were carefully peeled off from the MEA, and the cross-sections of the catalyst layer on the CCMs were prepared using an argon ion beam (IM4000, Hitachi High-Tech Corporation, Japan), and then observed using a scanning electron microscope (SEM, for Figures 4d, 5d, 6d,e and 8d) with a detector for energy-dispersive X-ray spectroscopy (EDX) (SU3500, Hitachi High-Tech Corporation, Japan; Xplore 30, Oxford Instruments Plc., UK), or cross-sectioned and observed using a focused ion beam (FIB) system with a scanning ion microscope (SIM, for Figure 4e) (FB2200, Hitachi High-Tech Corporation, Japan).

For some samples, the surface states of the elements in the catalyst layer were observed by X-ray photoelectron spectroscopy (XPS) (JPS-9010, JEOL Ltd., Japan) with Mg $K\alpha$ radiation. The obtained spectra were analyzed with the JEOL SpecSurf software package to apply a Shirley background subtraction. The binding energy (BE) was calibrated using the Au $4f_{7/2}$ peak (BE = 83.3 eV) of a gold wire as a reference.

3. RESULTS AND DISCUSSION

3.1. Initial MEA Performance. Figure 2 shows the initial MEA performance of each catalyst. Given the importance of operating at high current densities for the commercial deployment of AEMWE, we performed the polarization tests up to high current densities (4 A cm^{-2}).²³ Figure 2a shows the polarization curves of each catalyst. The electrolysis voltages before the durability test increased in the order $\text{IrO}_x < \text{NiCoMoO}_x < \text{NiCoO}_x \approx \text{NiFeO}_x$. Figure 2b shows the high frequency resistances (HFRs) of each catalyst. The initial HFRs increased in the $\text{IrO}_x < \text{NiFeO}_x < \text{NiCoMoO}_x < \text{NiCoO}_x$. Among the Ni-based catalysts, NiFeO_x showed the lowest HFR, while NiCoO_x had the highest, with NiCoMoO_x falling in between. Among all of the catalysts, IrO_x had the lowest HFR. The HFRs are the intersection of the real axis in the Cole–Cole plot of the impedance measurement, so the HFRs are the sum of the membrane resistance, catalyst layer resistances, PTLs resistances, and contact resistance at each

interface. Since the membrane, cathode catalyst layer, PTLs, and cell clamping pressure are the same for each MEA, the difference in HFRs is thought to depend on the difference in the anode catalyst layer resistance. Table 1 shows the

Table 1. Electronic Conductivities and BET Surface Areas of IrO_x , NiCoO_x , NiCoMoO_x , and NiFeO_x Catalyst

	electronic conductivity/ S cm^{-1}	BET surface area/ $\text{m}^2 \text{ g}^{-1}$
IrO_x	0.19	100
NiCoO_x	0.17	7.75
NiCoMoO_x	15	29.9
NiFeO_x	40	6.58

electronic conductivity and BET surface area of each anode catalyst. Note that the catalyst powder was used before grinding by ball milling for the conductivity measurements, while the milled catalysts were used for the MEAs. The order of HFRs for the Ni-based catalysts was consistent with the trend in the conductivities of the catalyst powders, but the HFRs calculated from the conductivities and the catalyst layer thicknesses (Table 3) did not match the actual HFRs. In addition, although the conductivity of IrO_x would be expected to result in the highest HFR, it actually showed the lowest. In this way, a possible reason for why the HFRs estimated from the conductivity did not match the actual HFRs is that the catalysts were partially crushed by the ball milling process, and the morphologies of the catalysts may have differed between the time of physical property measurement and the time of catalyst layer formation. In addition, the reason for the lowest HFR of IrO_x may be attributed to the thinner catalyst layer and smaller catalyst loading compared to the Ni-based catalysts (Table 3). Figure 2c,d show the *iR*-free Tafel plots using HFR and an enlarged view of the Tafel region ($0.01\text{--}0.1 \text{ A cm}^{-2}$), respectively. The inset in Figure 2d shows the anodic potential at 10 mA cm^{-2} for each catalyst in the RDE measurements.

The Tafel slopes for the Ni-based catalysts were all similar, approximately 70 mV dec^{-1} . The *iR*-free cell voltage at 10 mA cm^{-2} was lowest for IrO_x , followed by NiCoMoO_x , NiCoO_x , and finally NiFeO_x . This order was consistent with that of the RDE measurement of each individual catalyst.^{19–21} Figure 2e shows the relationship between the BET surface area of each catalyst and the deviation from the Tafel slopes at a current density of 2 A cm^{-2} ($\eta_{\text{mass}}@2 \text{ A cm}^{-2}$) in Figure 2c. The BET surface areas of the Ni-based catalysts were all less than that of IrO_x but the η_{mass} was better than that of IrO_x . The Ni-based oxide catalysts prepared by the flame pyrolysis method have the fused-aggregate network structure in which the nearest neighboring nanoparticles are connected, considered to be favorable for constructing both electronic conductive and gas diffusion pathways.¹⁹ Many gas diffusion pathways were formed by the Ni-based catalysts due to the unique fused-aggregate network structure, which is considered to enhance mass transport. We believe that these fused-aggregate network structures (see Figure S1) contributed to the low η_{mass} effect. Figure 2f shows the relationship between mass activity at 1.45 V and the BET surface area of each catalyst. The inset in Figure 2f is an enlarged view of the area with low BET surface area. The mass activity showed an increasing trend with increasing BET surface area. For the Ni-based catalysts, mass activity and BET surface area showed a linearly increasing trend. Since the Tafel slopes of the Ni-based catalysts were all approximately the same, it is considered that the difference in mass activity of the Ni-based catalysts can be attributed to the difference in reaction area due to the BET surface area. Therefore, it is expected that even higher *I*–*V* performance can be achieved by developing Ni-based catalysts with the fused-aggregate network structure and even higher BET surface areas.

3.2. Durability and Final MEA Performance. Hydrogen production using fluctuating power sources such as solar and

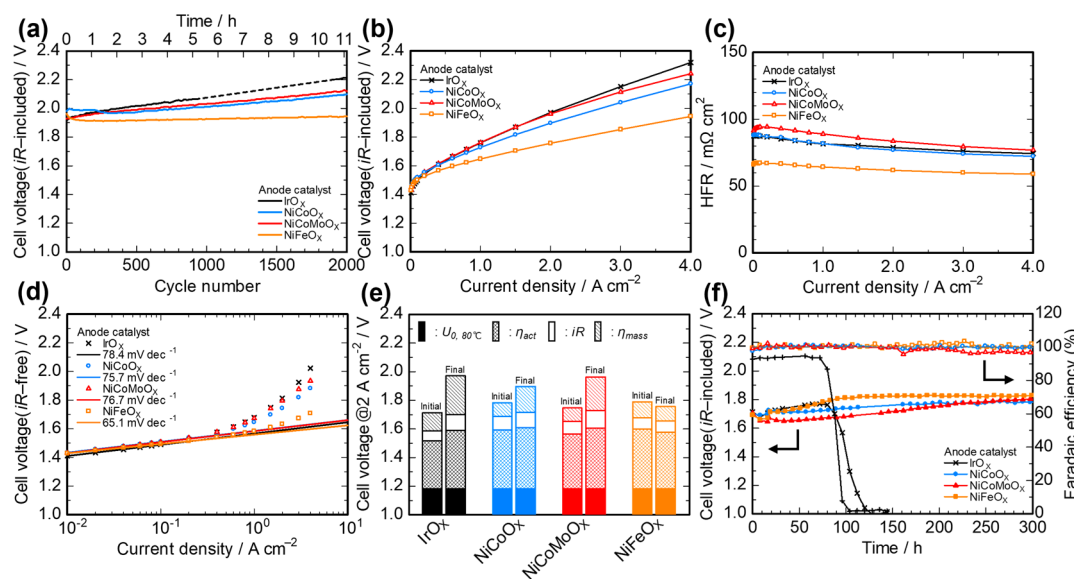


Figure 3. Durability and final performance of MEA using different anode catalysts (IrO_x , NiCoO_x , NiCoMoO_x , NiFeO_x) at 80°C with 1 M KOH solution. (a) Cell voltage changes at a current density of 4 A cm^{-2} during the start (4 A cm^{-2} , 10 s)–stop (0.1 V , 10 s) 2000-cycle accelerated degradation test, (b) polarization curves, (c) high frequency resistances, (d) *iR*-free Tafel plots, (e) breakdown of the various overpotentials in the cell voltage at a current density of 2 A cm^{-2} for the initial and final MEAs respectively, and (f) cell voltage changes and Faradaic efficiency calculated from generated O_2 at a current density of 1 A cm^{-2} during the load fluctuation ($0.04\text{--}2 \text{ A cm}^{-2}$)–constant (1 A cm^{-2} , 7.5 h) current 40-cycle durability test.

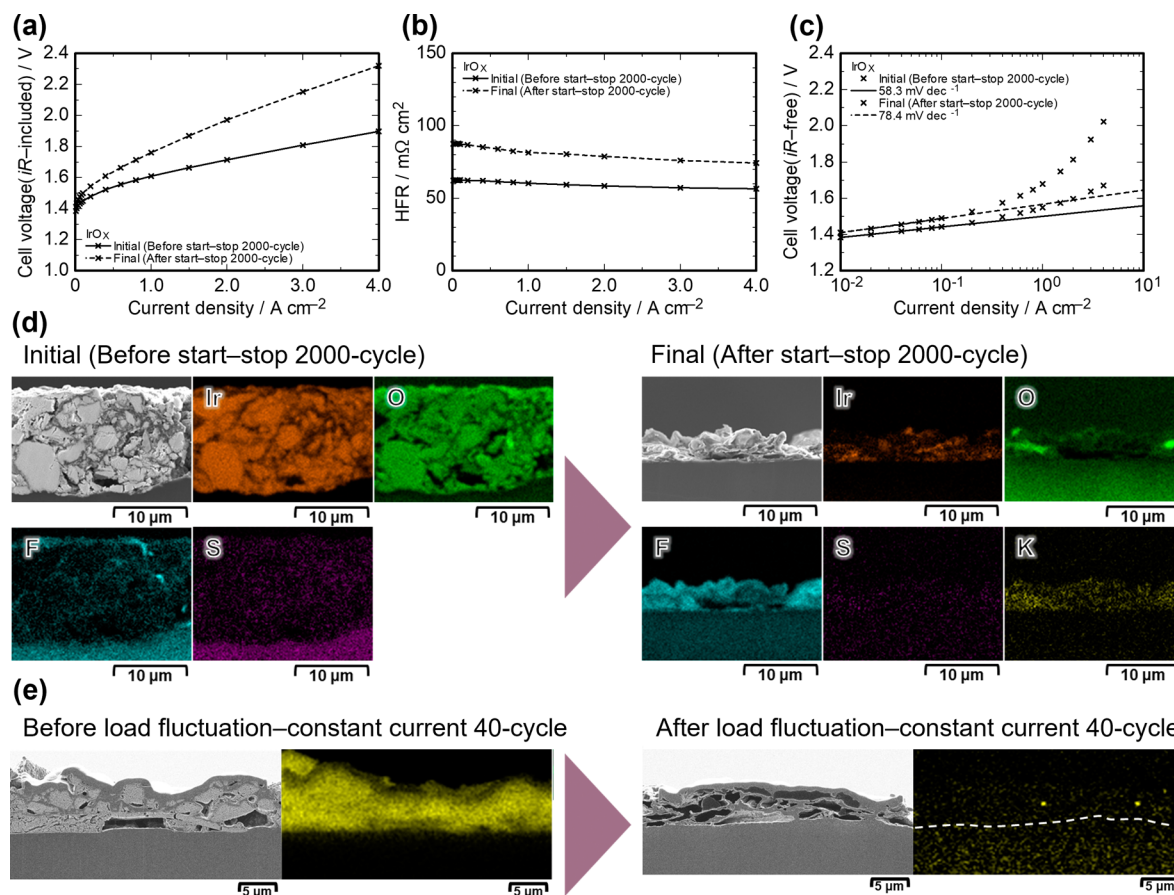


Figure 4. Performance changes in MEA using IrO_x as an anode catalyst for (a) polarization curves, (b) high frequency resistances, and (c) iR -free Tafel plots at 80 °C with 1 M KOH solution. (d) Cross-sectional SEM images and EDX mapping of the initial and final catalyst layers of IrO_x for start (4 A cm^{-2} , 10 s)–stop (0.1 V, 10 s) 2000-cycle accelerated degradation test, and (e) FIB–SIM images and EDX mapping of catalyst layers of IrO_x before and after load fluctuation (0.04–2 A cm^{-2})–constant (1 A cm^{-2} , 7.5 h) current 40-cycle durability test.

wind power is expected to be a low-cost hydrogen production method; thus, it is important that the water electrolysis cell can operate stably over a widely fluctuating power range.³ Therefore, we conducted a durability test following the start–stop accelerated degradation test protocol for PEMWE, proposed by Mitsubishi et al., repeating 2000 cycles of 10 s of high current load (4 A cm^{-2}) and 10 s at near zero current (0.1 V) (Figure 1a).²² Here, the constant potential control step is assumed to be a situation in which water electrolysis stops due to the use of unstable renewable power, and the hydrogen at the cathode crosses over to the anode, causing the anode potential to drop to near 0 V.²² Figure 3a shows the cell voltage changes during the high current load in the start–stop accelerated degradation test. In addition, the actual logging data for the cell voltage and current density during the ADT from the first to the tenth cycle are shown in Figure S2. The dotted area for the IrO_x data during the test indicates that data logging had stopped. During 2000 cycles, the cell voltages increased significantly for IrO_x , followed by NiCoMoO_x and NiCoO_x . For NiFeO_x , the cell voltage decreased during the first 100 cycles and gradually increased thereafter. Regarding the decrease in cell voltage, the conditioning described in Section 2.3 was not fully completed in NiFeO_x , and it is likely that conditioning continued to progress even during the ADT. The degradation rates during the 500–2000 cycles were 0.133, 0.0871, 0.0803, and 0.0183 mV cycle^{-1} for IrO_x , NiCoMoO_x , NiCoO_x , and NiFeO_x , respectively. Figure 3b–d show the

final MEA performance of each catalyst. Figure 3b shows the polarization curves of each catalyst. The electrolysis voltages after the durability test increased in the order $\text{NiFeO}_x < \text{NiCoO}_x < \text{NiCoMoO}_x < \text{IrO}_x$. Figure 3c shows HFRs of each catalyst. The final HFRs increased in the order $\text{NiFeO}_x < \text{NiCoO}_x \approx \text{IrO}_x < \text{NiCoMoO}_x$. Figure 3d shows the iR -free Tafel plots of each catalyst. The Tafel slopes of IrO_x , NiCoMoO_x , and NiCoO_x , which showed large cell voltage increases in the durability test, were all slightly less than 80 mV dec^{-1} . On the other hand, the Tafel slope of NiFeO_x was approximately 65 mV dec^{-1} , the smallest value. NiFeO_x also showed the smallest deviation from the Tafel slope in the high current density region among all the catalysts. Figure 3e shows the breakdown of the various overpotentials in the cell voltage at a current density of 2 A cm^{-2} for the initial and final MEAs, respectively. U_0 shows the equilibrium potential at 80 °C (approximately 1.18 V), η_{act} shows the deviation from the equilibrium potential to the Tafel slope (activation overpotential), iR shows the product of the current density and the high-frequency resistance (resistance overpotential), and η_{mass} shows the deviation from the Tafel slope (concentration overpotential). Note that the above overpotentials include the same amount of cathode contribution. In IrO_x , η_{act} and η_{mass} increased significantly before and after the durability test, and iR also increased. In NiCoO_x , η_{mass} increased significantly before and after the durability test, and η_{act} and iR increased slightly. In NiCoMoO_x , η_{act} and η_{mass} increased significantly

Table 2. Electrochemical Parameters for MEAs Using Various Anode Catalysts (IrO_x , NiCoO_x , NiCoMoO_x , NiFeO_x) Before and After Start (4 a cm^{-2} , 10 s)–stop (0.1 V, 10 s) 2000-Cycle Accelerated Degradation Test at 80 °C with 1 M KOH Solution

	IrO_x		NiCoO_x		NiCoMoO_x		NiFeO_x	
	initial	final	initial	final	initial	final	initial	final
cell voltage@4 A cm^{-2} /V	1.90	2.32	1.98	2.17	1.94	2.24	1.98	1.94
η_{act} @2 A cm^{-2} /mV	334	407	410	424	382	423	414	395
Tafel slope/mV dec^{-1}	58.3	78.4	69.7	75.7	69.0	76.7	67.4	65.1
Tafel line shift@0.01 A cm^{-2} /ΔmV	+27.3		+1.65		+24.4		-15.1	
iR @2 A cm^{-2} /mV	117	158	140	154	134	167	128	124
ave HFR/mΩ	60.9	83.7	74.4	83.5	71.1	89.5	66.8	64.9
η_{mass} @2 A cm^{-2} /mV	79.0	223	48.0	135	47.4	189	63.3	54.7

Table 3. SEM–EDX Results for MEA Using Various Anode Catalysts (IrO_x , NiCoO_x , NiCoMoO_x , NiFeO_x) Before and after Start (4 a cm^{-2} , 10 s)–stop (0.1 V, 10 s) 2000-Cycle Accelerated Degradation Test at 80 °C with 1 M KOH Solution

	IrO_x		NiCoO_x		NiCoMoO_x		NiFeO_x	
	initial	final	initial	final	initial	final	initial	final
ave anode catalyst layer thickness/ μm	12.1	2.6	15.8	19.1	15.3	19.2	15.6	14.6
element (wt %)								
Ir	68.7	4.8						
Ni			60.2	55.6	59.2	43.5	63.3	56.4
Co			15.7	11.4	7.6	5.7		
Mo					9.6	2.4		
Fe							14.3	12.6
O	10.4	10.8	4.6	11.8	5.0	16.2	5.3	12.5
F	1.0	17.8	3.2	3.1	2.3	4.2	2.1	4.1
S	1.1	0.1	0.6	0.0	0.4	0.0	0.4	0.0
K	0.0	1.0	0.0	5.0	0.0	1.3	0.0	1.7

before and after the durability test, and iR also increased. In NiFeO_x , η_{act} decreased slightly before and after the durability test, and iR and η_{mass} did not change. In addition to the durability for startup and shutdown, the load fluctuation (0.04–2 A cm^{-2}) and constant (1 A cm^{-2} , 7.5 h) current 40-cycle durability test was also conducted (Figure 1b). This protocol is the one we have used in our previous investigations of the durability of electrolyte materials.^{26–29} Figure 3f shows the cell voltage changes at a constant current of 1 A cm^{-2} during the load fluctuation–constant current 40-cycle durability test. For IrO_x , the cell voltage decreased slightly during the first 8 h, increased thereafter, and then dropped sharply from the 80th hour onward. The gas production rate also decreased rapidly along with the cell voltage. In NiCoO_x , the cell voltage slightly decreased during the first 8 h and increased slowly thereafter. In the NiCoMoO_x , the cell voltage decreased in the first 16 h and increased thereafter. The gas production rate decreased gradually from the 150th hour. In NiFeO_x , the cell voltage slightly decreased in the first 8 h, increased until the 100th hour but remained constant thereafter. Note that the cell voltage temporarily increased at the 16th hour for the Ni-based catalyst, which was due to an impedance measurement during the test. We compared the initial and final MEA performance and catalyst layers in order to discuss how the MEAs changed during these durability tests.

3.3. Comparison of Both MEA Performance and the Post-Test Analysis Before and after the Durability Evaluation for Each Anode Catalyst. 3.3.1. IrO_x : Figure 4a–c show a comparison of the initial and final MEA performance of IrO_x in the start–stop accelerated degradation test. A comparison of the electrochemical parameters before and after the durability evaluations for IrO_x is shown in Table 2. Figure 4a presents a comparison of the polarization curves.

Compared to the initial I – V performance, the final I – V performance exhibited higher electrolysis voltage throughout the entire current density range, and the iR -included cell voltage at 4 A cm^{-2} increased from 1.90 V (@initial) to 2.32 V (@final). Figure 4b displays a comparison of the HFR values. The average HFR of the entire current density increased from 60.9 mΩ cm^2 (@initial) to 83.7 mΩ cm^2 (@final), and the iR at 2 A cm^{-2} increased from 117 mV to 158 mV. Figure 4c shows a comparison of iR -free Tafel plots. The Tafel slope increased from 58.3 mV dec^{-1} (@initial) to 78.4 mV dec^{-1} (@final), and the Tafel line shifted upward by 27.3 mV (@0.01 A cm^{-2}). The Tafel slopes ranged from 57.5 to 63.0 mV dec^{-1} depending on the calculated current density range, even for the same measurement (Figure S3). In addition, the Tafel slope varied from 60.7 to 67.4 mV dec^{-1} when five cells were measured with the same calculated current density range and the same MEA configuration (Figure S11). However, the increase in the Tafel slope from 58.3 mV dec^{-1} (initial) to 78.4 mV dec^{-1} (final) in the case of IrO_x is considered to be outside of these variations. Therefore, it is assumed that the reaction on the catalyst surface may have changed significantly in the start–stop accelerated degradation test. In addition, the upward shift of the Tafel line may be due to a decrease in the reaction area. These results caused the η_{act} at 2 A cm^{-2} to increase from 334 to 407 mV. Furthermore, the η_{mass} value at 2 A cm^{-2} increased significantly, from 79.0 to 223 mV. Figure 4d shows the cross-sectional SEM images and EDX mapping of the initial and final catalyst layer of IrO_x in the start–stop accelerated degradation test. The average thickness of the initial and final catalyst layers of IrO_x and the weight percentage of the elements at the center point of the catalyst layer are shown in Table 3. The average thickness of the initial catalyst layer was 12.1 μm , with abundant Ir and O associated

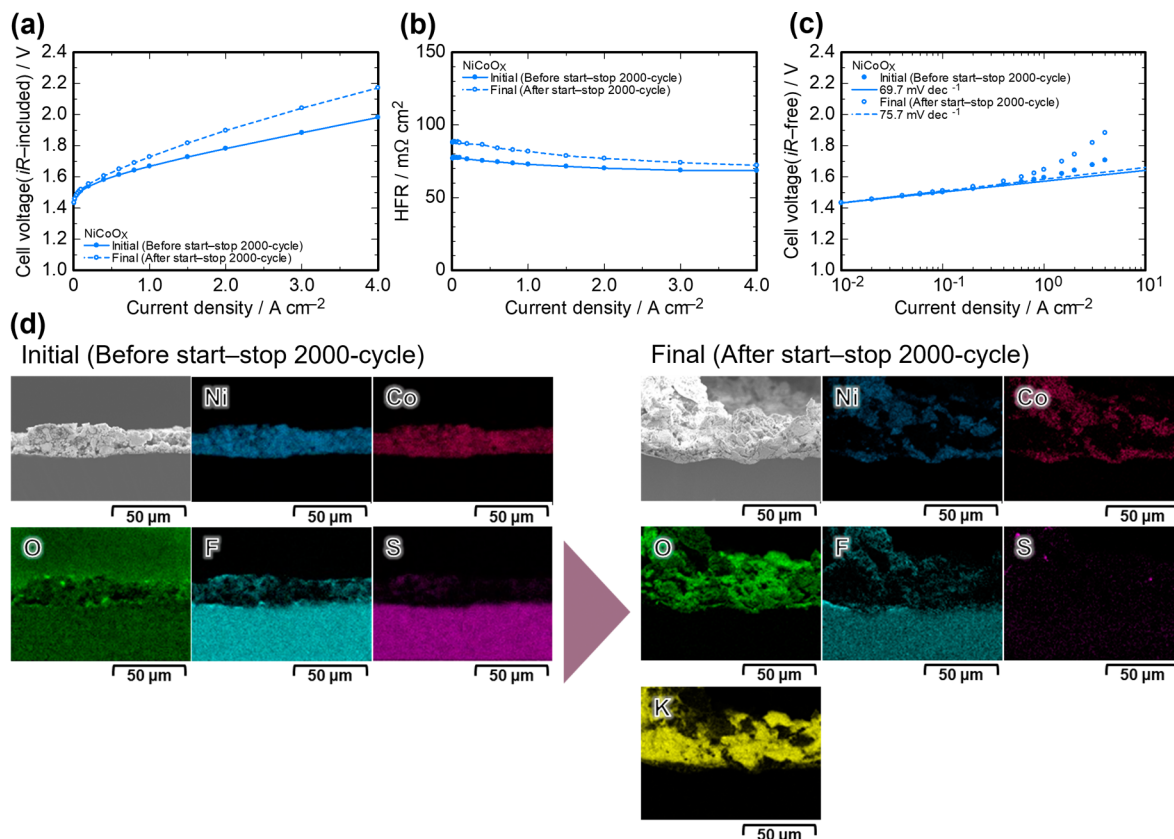


Figure 5. Performance changes in MEA using NiCoO_x as an anode catalyst for (a) polarization curves, (b) high frequency resistances, and (c) *iR*-free Tafel plots at 80 °C with 1 M KOH solution. (d) Cross-sectional SEM images and EDX mapping of the initial and final catalyst layers of NiCoO_x for start (4 A cm⁻², 10 s)—stop (0.1 V, 10 s) 2000-cycle accelerated degradation test.

with the catalyst, and F and S associated with the ionomer side chains and counterions.²³ In contrast, the average thickness of the final catalyst layer decreased to 2.6 μm, and Ir and S in the catalyst layer declined significantly, while K appeared. It has been reported that IrO_x may become unstable when it is used as a catalyst for the oxygen evolution reaction (OER) in alkaline media, due to the oxidation of the surface IrO_x to water-soluble IrO₄²⁻ or other solvated Ir (VI) ions.³⁰ In addition, the Ir Pourbaix diagram also suggests the possibility of IrO_x elution in the assumed OER region of AEMWE (Figure S4, The red double arrow in Figure S4 shows the assumed potential range of the IrO_x during the ADT).³¹ The decrease in S is attributed to the replacement of the MeSO₄⁻ ions, the counterions of the quaternary ammonium groups of the QPAF-4 ionomer, with hydroxide or carbonate ions, and the appearance of K is attributed to the residual KOH electrolyte in the catalyst layer. From these results and the Pourbaix diagram, it is considered that Ir leached out and formed voids in the catalyst layer during the start–stop accelerated degradation test, causing a decrease in the reaction area and stagnation of the generated gas bubbles.

Figure 4e shows FIB–SIM images and EDX mapping of Ir in the catalyst layer before and after the load fluctuation–constant current 40-cycle durability test. The average catalyst layer thickness before the durability test was 5.8 μm, with abundant Ir observed in the catalyst layer. After the durability test, Ir was not observed in the catalyst layer but was found in the electrolyte membrane. Based on these observations, it is considered that Ir was completely leached out during the load fluctuation–constant current 40-cycle durability test, causing

the anode catalyst layer to become thin. This resulted in the anode PTL directly contacting the electrolyte membrane, eventually breaking through the membrane and contacting the cathode PTL, leading to a short circuit. Consequently, the cell voltage and gas production rate were considered to have dropped significantly, as seen in Figure 3f.

3.3.2. NiCoO_x. Figure 5a–c show a comparison of the initial and final MEA performance of NiCoO_x in the start–stop accelerated degradation test. A comparison of the initial and final electrochemical parameters of NiCoO_x is shown in Table 2. Figure 5a presents a comparison of the polarization curves. Compared to the initial *I*–*V* performance, the final *I*–*V* performance exhibited higher electrolysis voltages at higher current density, and the *iR*-included cell voltage at 4 A cm⁻² increased from 1.98 V (@initial) to 2.17 V (@final). Figure 5b displays a comparison of the HFR values. The average HFR of the entire current density increased from 74.4 mΩ cm² (@initial) to 83.5 mΩ cm² (@final), and the *iR* at 2 A cm⁻² increased from 140 to 154 mV. Figure 5c shows a comparison of *iR*-free Tafel slopes, which increased from 69.7 mV dec⁻¹ (@initial) to 75.7 mV dec⁻¹ (@final), and the Tafel line shifted upward slightly by 1.65 mV (@0.01 A cm⁻²). However, the Tafel slope varied from 65.9 to 72.5 mV dec⁻¹ depending on the calculated current density range for the same measurement results (Figure S5). In addition, the Tafel slope varied from 60.7 to 67.4 mV dec⁻¹ when five cells were measured with the same calculated current density range and the same MEA configuration (Figure S11). Therefore, the increase in the Tafel slope from 69.7 mV dec⁻¹ (initial) to 75.7 mV dec⁻¹ (final) in the case of NiCoO_x is expected to be

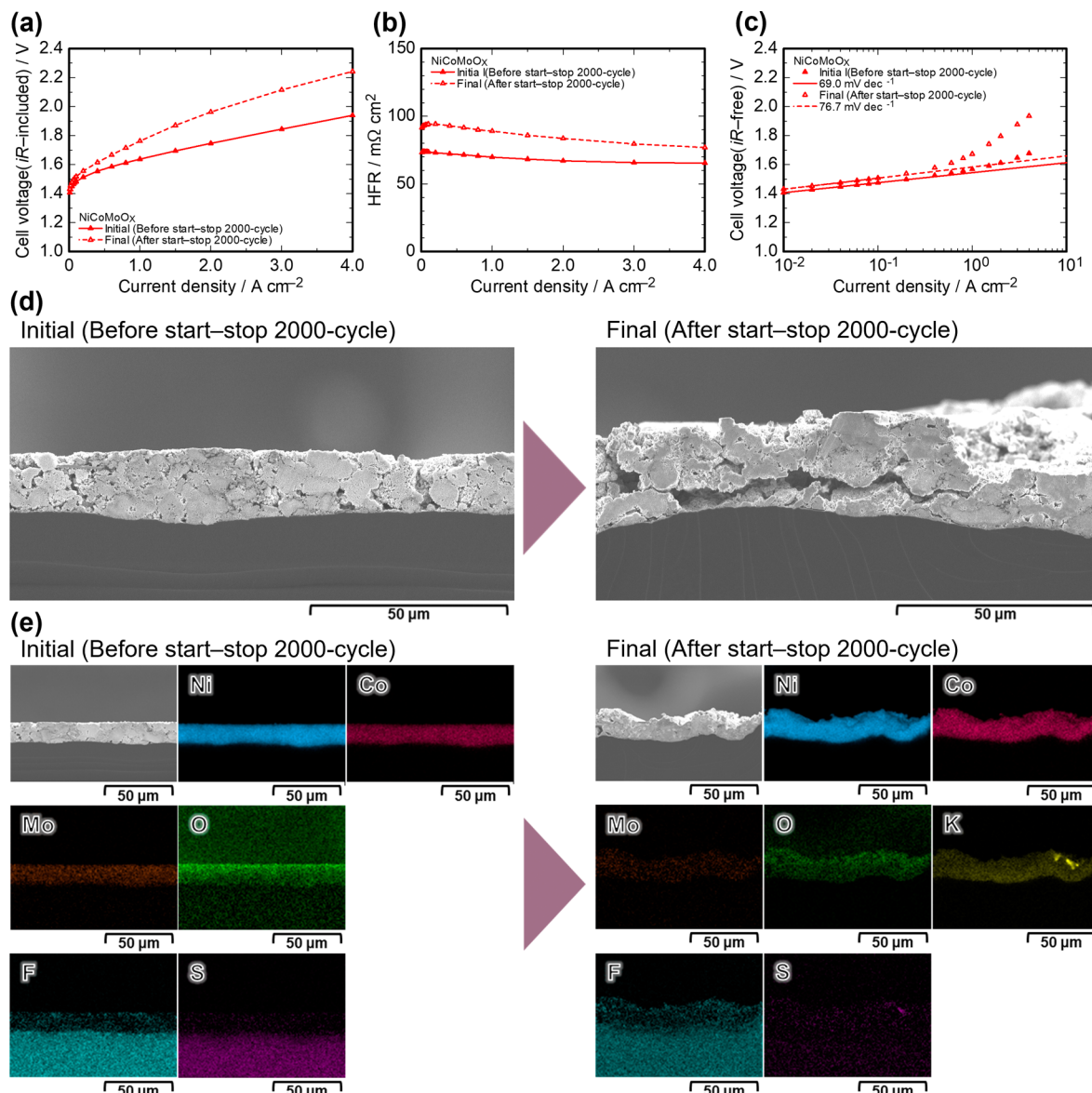


Figure 6. Performance changes in MEA using NiCoMoO_x as an anode catalyst for (a) polarization curves, (b) high frequency resistances, and (c) iR -free Tafel plots at 80 °C with 1 M KOH solution. (d) Cross-sectional SEM images, and (e) EDX mapping of the initial and final catalyst layers of NiCoMoO_x for start (4 $A\text{ cm}^{-2}$, 10 s)–stop (0.1 V, 10 s) 2000-cycle accelerated degradation test.

within the measurement error range, and it is considered that the reaction on the catalyst surface had not changed significantly in the start–stop accelerated degradation test. In addition, considering that the upward shift of the Tafel line was only slight, it is also suggested that the reaction area did not change greatly. On the other hand, the η_{mass} at 2 $A\text{ cm}^{-2}$ increased significantly from 48.0 to 135 mV. Figure 5d shows the cross-sectional SEM images and EDX mapping of the initial and final catalyst layer of NiCoO_x in the start–stop accelerated degradation test. The average thickness of the initial and final catalyst layers of NiCoO_x and the weight percentage of the elements at the center point of the catalyst layer are shown in Table 3. The average thickness of the initial catalyst layer was 15.8 μm , with abundant Ni, Co and O associated with the catalyst, and F and S associated with the ionomer side chains and counterions.^{19,23} The average thickness of the final catalyst layer was 19.1 μm , and Ni, Co, O associated with the catalyst and F associated with the

ionomer side chain were still found, while the S associated with the ionomer counterion decreased, and a large amount of K and O appeared. The decrease in S was attributed to the replacement of the MeSO_4^- ions with hydroxide or carbonate ions, and the large amount of K and O appearance was attributed to the residual large amount of KOH electrolyte in the catalyst layer. Pourbaix diagrams for Ni and Co suggest that they are both unlikely to form water-soluble cations in the assumed OER region of AEMWE (Figures S6 and S7, the red double arrows in Figures S6 and S7 show the assumed potential range of the Ni-based catalysts and NiCoO_x during the ADT, respectively), and furthermore, it has been reported that the potential-dependent dissolution rates of NiO_xH_y and CoO_xH_y at OER potentials are 3 orders of magnitude lower than that of FeO_xH_y , and thus these catalysts are far more stable.^{31–33} Our results that Ni and Co were observed in the final anode catalyst layer are consistent with these facts. As the anode NiCoO_x catalyst did not change dramatically, with

negligible leaching, it is considered that the Tafel slope in Figure 5c did not change significantly before and after the durability test. However, the reason why the final η_{mass} was larger than the initial η_{mass} at high current densities has not yet been clarified. During the durability test, the structure of the catalyst layer and the catalyst layer-PTL interface may have changed, and voids may have formed. This may have caused the generated gas to stagnate, but further investigation is required to understand the mechanism.

3.3.3. NiCoMoO_X. Figure 6a–c show a comparison of the initial and final MEA performance of NiCoMoO_X in the start–stop accelerated degradation test. A comparison of the initial and final electrochemical parameters of NiCoMoO_X is shown in Table 2. Figure 6a presents a comparison of the polarization curves. Compared to the initial I – V performance, the final I – V performance exhibited higher electrolysis voltage throughout the entire current density, and the iR -included cell voltage at 4 A cm^{-2} increased from 1.94 V (@initial) to 2.24 V (@final). Figure 6b displays a comparison of HFRs. The average HFR of the entire current density increased from 71.1 $\text{m}\Omega \text{ cm}^2$ (@initial) to 89.5 $\text{m}\Omega \text{ cm}^2$ (@final), and the iR at 2 A cm^{-2} increased from 134 mV to 167 mV. Figure 6c shows a comparison of iR -free Tafel slopes, which increased from 69.0 mV dec^{-1} (@initial) to 76.7 mV dec^{-1} (@final), and the Tafel line shifted upward by 24.4 mV (@0.01 A cm^{-2}). However, the Tafel slope varied from 68.6 to 70.2 mV dec^{-1} depending on the calculated current density range for the same measurement results (Figure S8). In addition, the Tafel slope varied from 60.7 to 67.4 mV dec^{-1} when five cells were measured with the same calculated current density range and the same MEA configuration (Figure S11). Therefore, the increase in the Tafel slope from 69.0 mV dec^{-1} (initial) to 76.7 mV dec^{-1} (final) in the case of NiCoMoO_X is expected to be within the measurement error range, and it is considered that the reaction on the catalyst surface had not changed significantly in the start–stop accelerated degradation test. On the other hand, considering the upward shift of the Tafel line, it is suggested that the reaction area decreased. In addition, the η_{mass} at 2 A cm^{-2} increased significantly from 47.4 to 189 mV. Figure 6d,e shows the cross-sectional SEM images and EDX mapping, respectively, of the initial and final catalyst layer of NiCoMoO_X in the start–stop accelerated degradation test. The average thicknesses of the initial and final catalyst layers of NiCoMoO_X and the weight percentages of the elements at the center point of the catalyst layer are shown in Table 3. The average thickness of the initial catalyst layer was 15.3 μm , with abundant Ni, Co, Mo, and O associated with the catalyst, and F and S associated with the ionomer side chains and counterions.^{21,23} The average thickness of the final catalyst layer was 19.2 μm , and Ni, Co, O, and F were still found, while S and Mo decreased, and K appeared. The decrease in S is attributed to the replacement of the MeSO_4^- ions with hydroxide or carbonate ions, and the K appearance is attributed to the residual KOH electrolyte in the catalyst layer. Figure 7 shows the comparison of Mo 3d XPS spectra of NiCoMoO_X before and after the load fluctuation–constant current 40-cycle durability test. Before the test, typical Mo peaks centered at 238.2 and 235.1 eV were observed in the catalyst layer, but after the test, none of these peaks were observed. It has been reported that Mo may become less stable when it is used as a catalyst for the OER in alkaline media, due to the oxidation of the low-valent Mo species to water-soluble Mo⁶⁺ compounds.³⁴ In addition, the Mo Pourbaix

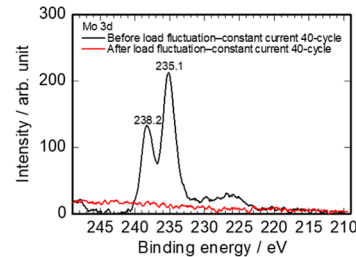


Figure 7. Comparison of the Mo 3d XPS spectra of NiCoMoO_X before and after load fluctuation ($0.04\text{--}2 \text{ A cm}^{-2}$)–constant (1 A cm^{-2} , 7.5 h) current 40-cycle durability test.

diagram also suggests the possibility of Mo elution in the assumed OER region of AEMWE (Figure S9).³⁵ From these results and the Pourbaix diagram, it is considered that Mo on the catalyst surface oxidized and dissolved as an MoO_4^{2-} species during the durability test, resulting in a decrease in the reaction area.^{21,34,36} The partial dissolution of Mo may have weakened the catalyst layer, causing the voids seen in Figure 6d (right), which may have led to the stagnation of the generated gas (and increase in η_{mass}).

3.3.4. NiFeO_X. Figure 8a–c show a comparison of the initial and final MEA performance of NiFeO_X in the start–stop accelerated degradation test. A comparison of the initial and final electrochemical parameters of NiFeO_X is shown in Table 2. Figure 8a presents a comparison of the polarization curves. Compared to the initial I – V performance, the final I – V performance exhibited lower electrolysis voltages throughout the entire current density, and the iR -included cell voltage at 4 A cm^{-2} decreased from 1.98 V (@initial) to 1.94 V (@final). Figure 8b displays a comparison of the HFR values. The average HFR of the entire current density decreased slightly from 66.8 $\text{m}\Omega \text{ cm}^2$ (@initial) to 64.9 $\text{m}\Omega \text{ cm}^2$ (@final), and the iR at 2 A cm^{-2} also decreased slightly from 128 to 124 mV. Figure 8c shows a comparison of iR -free Tafel slope, which decreased from 67.4 mV dec^{-1} (@initial) to 65.1 mV dec^{-1} (@final), and the Tafel line shifted downward by 15.1 mV (@0.01 A cm^{-2}). However, the Tafel slope varied from 65.4 to 72.1 mV dec^{-1} depending on the calculated current density range for the same measurement results (Figure S10). In addition, the Tafel slope varied from 60.7 to 67.4 mV dec^{-1} when five cells were measured with the same calculated current density range and the same MEA configuration (Figure S11). Therefore, the decrease in the Tafel slope from 67.4 mV dec^{-1} (initial) to 65.1 mV dec^{-1} (final) in the case of NiFeO_X is expected to be within the measurement error range, and it is considered that the reaction on the catalyst surface had not changed significantly in the start–stop accelerated degradation test. On the other hand, considering the downward shift of the Tafel line, it is suggested that the reaction area increased. In addition, the η_{mass} value at 2 A cm^{-2} decreased from 63.3 to 54.7 mV. Figure 8d shows the cross-sectional SEM images and EDX mapping of the initial and final catalyst layer of NiFeO_X in the start–stop accelerated degradation test. The average thickness of the initial and final catalyst layers of NiFeO_X and the weight percentage of the elements at the center point of the catalyst layer are shown in Table 3. The average thickness of the initial catalyst layer was 15.6 μm , with abundant Ni, Fe, and O associated with the catalyst, and F and S associated with the ionomer side chains and counterions.^{20,23} The average thickness of the final catalyst layer was 14.6 μm , and the Ni, Fe, O, and F were still found, while S decreased, and K appeared.

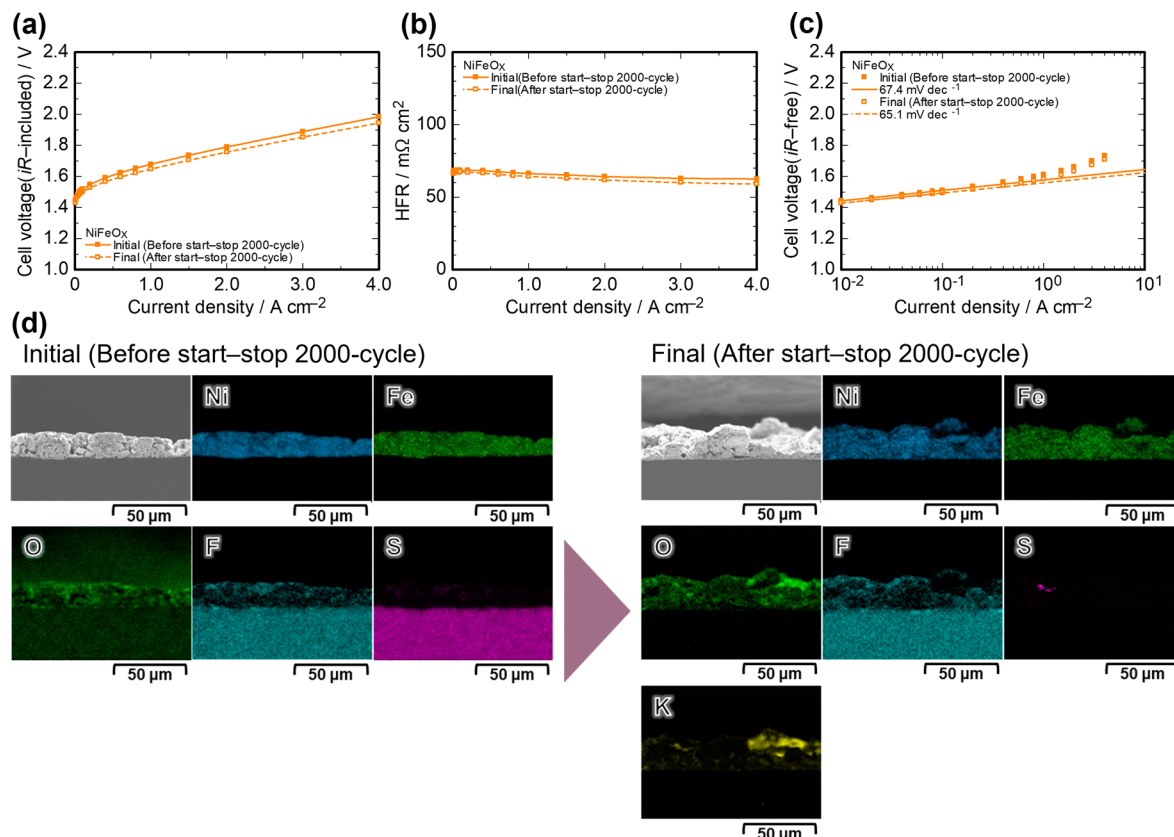


Figure 8. Performance changes in MEA using NiFeO_x as an anode catalyst for (a) polarization curves, (b) high frequency resistances, and (c) $i\text{R}$ -free Tafel plots at 80 °C with 1 M KOH solution. (d) Cross-sectional SEM images and EDX mapping of the initial and final catalyst layers of NiFeO_x for start (4 A cm⁻², 10 s)–stop (0.1 V, 10 s) 2000-cycle accelerated degradation test.

The decrease in S is attributed to the replacement of the MeSO_4^- ions with hydroxide or carbonate ions, and the K appearance is attributed to the residual KOH electrolyte in the catalyst layer. According to the Pourbaix diagram, Fe is likely to dissolve in the OER assumed region in AEMWE (Figure S12, the red double arrow in Figure S12 shows the assumed potential range of the NiFeO_x during the ADT), and the dissolution of Fe occurs in NiFe-based electrocatalysts during alkaline water electrolysis.^{31,37} In addition, it has been reported that the potential-dependent dissolution rates of FeO_xH_Y at OER potentials is 3 orders of magnitude higher than NiO_xH_Y and CoO_xH_Y .³³ By contrast, in this study, abundant Fe was found in the catalyst layer even after 2000 cycles of startup and shutdown accelerated degradation tests, and surprisingly, the MEA performance was somewhat improved. In our NiFeO_x catalyst, the Fe component is located in the core and covered with an Ni or NiO_x shell, which suppresses the dissolution of Fe. We believe that this effect is amply demonstrated. However, the partial dissolution of Fe on the catalyst surface during the durability test, leading to the formation of higher activity sites and improved MEA performance (increased reaction area), is one of the currently considered possibilities, but further investigation is needed.

4. CONCLUSIONS

We investigated the MEA performance and durability of AEMWE single cells using the in-house developed Ni-based oxide catalysts (NiCoO_x , NiCoMoO_x , NiFeO_x) for the anode, and the in-house developed anion exchange ionomer (QPAF-4) for both the membrane and the catalyst layer binder.

According to the initial MEA performance evaluation up to a current density of 4 A cm⁻², although the electrolytic voltage itself was higher for the Ni-based catalysts than for the commercial IrO_x , the $\eta_{\text{mas}}@2 \text{ A cm}^{-2}$ value was superior to that of IrO_x . This suggests that the fused-aggregate network structure, in which neighboring nanoparticles are connected, is effective in enhancing mass transport even at current densities of several A cm⁻². Although the Tafel slopes of the Ni-based catalysts were nearly identical at about 70 mV dec⁻¹, the mass activities and BET surface areas exhibited a linear correlation. According to the results of the start (4 A cm⁻², 10 s)–stop (0.1 V, 10 s) 2000 cycles accelerated degradation test, the cell voltage of IrO_x significantly increased during the test, while the cell voltage of NiFeO_x was extremely stable throughout the test, and no significant changes in the cross-section of the catalyst layer were observed before and after the test. Based on these results, we propose a design guideline, specifically, that it is important to select an NiFe material and expand its specific surface area (increase the number of active sites) toward the development of electrocatalysts with high performance and durability. These promising results are expected to contribute significantly toward the development of low-cost, high-performance, and durability AEMWE stacks for commercial applications.

ASSOCIATED CONTENT

Supporting Information

The Supporting Information is available free of charge at <https://pubs.acs.org/doi/10.1021/acsaem.5c00214>.

TEM images of Ni-based catalysts, the synthetic procedure of the QPAF-4, logging data during the ADT, deviations of Tafel slopes depending on the calculated current density range, Tafel slope based on $n = 5$ averaged using independent MEAs, Pourbaix diagrams (PDF)

AUTHOR INFORMATION

Corresponding Author

Makoto Uchida — *Hydrogen and Fuel Cell Nanomaterials Center, University of Yamanashi, Kofu 400-0021, Japan;* orcid.org/0000-0002-7847-3727; Email: uchidam@yamanashi.ac.jp

Authors

Soichiro Natori — *Integrated Graduate School of Medicine and Engineering and Agricultural Sciences, University of Yamanashi, Kofu 400-8511, Japan*

Sayaka Takahashi — *Integrated Graduate School of Medicine and Engineering and Agricultural Sciences, University of Yamanashi, Kofu 400-8511, Japan*

Toshio Iwataki — *Hydrogen and Fuel Cell Nanomaterials Center, University of Yamanashi, Kofu 400-0021, Japan*

Takayuki Asakawa — *Hydrogen and Fuel Cell Nanomaterials Center, University of Yamanashi, Kofu 400-0021, Japan*

Guoyu Shi — *Hydrogen and Fuel Cell Nanomaterials Center, University of Yamanashi, Kofu 400-0021, Japan;* orcid.org/0000-0002-5596-585X

Katsuyoshi Kakinuma — *Hydrogen and Fuel Cell Nanomaterials Center, University of Yamanashi, Kofu 400-0021, Japan; Clean Energy Research Center, University of Yamanashi, Kofu 400-8510, Japan;* orcid.org/0002-5010-994X

Kenji Miyatake — *Hydrogen and Fuel Cell Nanomaterials Center, University of Yamanashi, Kofu 400-0021, Japan; Clean Energy Research Center, University of Yamanashi, Kofu 400-8510, Japan; Department of Applied Chemistry, Waseda University, Tokyo 169-8555, Japan;* orcid.org/0000-0001-5713-2635

Complete contact information is available at:

<https://pubs.acs.org/10.1021/acsaem.5c00214>

Author Contributions

The manuscript was written through contributions of all authors. All authors have given approval to the final version of the manuscript.

Notes

The authors declare no competing financial interest.

ACKNOWLEDGMENTS

This work was partially based on results obtained from project JPNP20003, commissioned by the New Energy and Industrial Technology Development Organization (NEDO) and on GteX Program Japan Grant Number JPMJGX23H2.

REFERENCES

- (1) Zhu, J.; Hu, L.; Zhao, P.; Lee, L. Y. S.; Wong, K.-Y. Recent Advances in Electrocatalytic Hydrogen Evolution Using Nanoparticles. *Chem. Rev.* **2020**, *120* (2), 851–918.
- (2) Yu, M.; Budiyanto, E.; Tüysüz, H. Principles of Water Electrolysis and Recent Progress in Cobalt-, Nickel-, and Iron-Based Oxides for the Oxygen Evolution Reaction. *Angew. Chem., Int. Ed.* **2022**, *61* (1), No. e202103824.
- (3) Kojima, H.; Nagasawa, K.; Todoroki, N.; Ito, Y.; Matsui, T.; Nakajima, R. Influence of Renewable Energy Power Fluctuations on Water Electrolysis for Green Hydrogen Production. *Int. J. Hydrogen Energy* **2023**, *48* (12), 4572–4593.
- (4) Ehlers, J. C.; Feidenhans'l, A. A.; Therkildsen, K. T.; Larrazábal, G. O. Affordable Green Hydrogen from Alkaline Water Electrolysis: Key Research Needs from an Industrial Perspective. *ACS Energy Lett.* **2023**, *8* (3), 1502–1509.
- (5) Shi, G.; Tano, T.; Tryk, D. A.; Uchiyama, T.; Iiyama, A.; Uchida, M.; Terao, K.; Yamaguchi, M.; Tamoto, K.; Uchimoto, Y.; Kakinuma, K. Nanorod Structuring of IrO_x on a Unique Microstructure of Sb-Doped Tin Oxide to Dramatically Boost the Oxygen Evolution Reaction Activity for PEM Water Electrolysis. *ACS Catal.* **2023**, *13* (18), 12299–12309.
- (6) Kumar, S. S.; Lim, H. An Overview of Water Electrolysis Technologies for Green Hydrogen Production. *Energy Rep.* **2022**, *8*, 13793–13813.
- (7) Yue, M.; Lambert, H.; Pahon, E.; Roche, R.; Jemei, S.; Hissel, D. Hydrogen Energy Systems: A Critical Review of Technologies, Applications, Trends and Challenges. *Renew. Sustain. Energy Rev.* **2021**, *146*, 111180.
- (8) Park, E. J.; Arges, C. G.; Xu, H.; Kim, Y. S. Membrane Strategies for Water Electrolysis. *ACS Energy Lett.* **2022**, *7* (10), 3447–3457.
- (9) Chen, B.; Biancolli, A. L. G.; Radford, C. L.; Holdcroft, S. Stainless Steel Felt as a Combined OER Electrocatalyst/Porous Transport Layer for Investigating Anion-Exchange Membranes in Water Electrolysis. *ACS Energy Lett.* **2023**, *8* (6), 2661–2667.
- (10) Galkina, I.; Faid, A. Y.; Jiang, W.; Scheepers, F.; Borowski, P.; Sunde, S.; Shviro, M.; Lehnert, W.; Mechler, A. K. Stability of Ni–Fe-Layered Double Hydroxide Under Long-Term Operation in AEM Water Electrolysis. *Small* **2024**, *20* (26), 2311047.
- (11) Li, Q.; Villarino, A. M.; Peltier, C. R.; Macbeth, A. J.; Yang, Y.; Kim, M.-J.; Shi, Z.; Krumov, M. R.; Lei, C.; Rodríguez-Calero, G. G.; Soto, J.; Yu, S.-H.; Mutolo, P. F.; Xiao, L.; Zhuang, L.; Muller, D. A.; Coates, G. W.; Zelenay, P.; Abruna, H. D. Anion Exchange Membrane Water Electrolysis: The Future of Green Hydrogen. *J. Phys. Chem. C* **2023**, *127* (17), 7901–7912.
- (12) Narayanaru, S.; Miyanishi, S.; Kuroki, H.; Anilkumar, G. M.; Yamaguchi, T. Start–Stop Cyclic Durability Analysis of Membrane–Electrode Assemblies Using Polyflourene-Based Electrolytes for an Anion-Exchange Membrane Water Electrolyzer. *ACS Sustain. Chem. Eng.* **2023**, *11* (25), 9295–9302.
- (13) López-Fernández, E.; Gil-Rostra, J.; Espinós, J. P.; González-Elipe, A. R.; de Lucas Consuegra, A.; Yubero, F. Chemistry and Electrocatalytic Activity of Nanostructured Nickel Electrodes for Water Electrolysis. *ACS Catal.* **2020**, *10* (11), 6159–6170.
- (14) Du, N.; Roy, C.; Peach, R.; Turnbull, M.; Thiele, S.; Bock, C. Anion-Exchange Membrane Water Electrolyzers. *Chem. Rev.* **2022**, *122* (13), 11830–11895.
- (15) Hu, C.; Lee, Y. J.; Ma, Y.; Zhang, X.; Jung, S. W.; Hwang, H.; Cho, H. K.; Kim, M.-G.; Yoo, S. J.; Zhang, Q.; Lee, Y. M. Advanced Patterned Membranes for Efficient Alkaline Membrane Electrolyzers. *ACS Energy Lett.* **2024**, *9* (3), 1219–1227.
- (16) Park, J. E.; Park, S.; Kim, M.-J.; Shin, H.; Kang, S. Y.; Cho, Y.-H.; Sung, Y.-E. Three-Dimensional Unified Electrode Design Using a NiFeOOH Catalyst for Superior Performance and Durable Anion-Exchange Membrane Water Electrolyzers. *ACS Catal.* **2022**, *12* (1), 135–145.
- (17) Lee, C.; Yun, Y. H.; Kim, S.-H.; Doo, G.; Lee, S.; Park, H.; Park, Y.; Shin, J.; Cho, H.-S.; Kim, S.-K.; Cho, E.; Jung, C.; Kim, M. Structural and Compositional Optimization of Fe–Co–Ni Ternary Amorphous Electrocatalysts for Efficient Oxygen Evolution in Anion Exchange Membrane Water Electrolysis. *Small* **2025**, *21* (4), 2405468.
- (18) Yang, X.; Liang, J.; Shi, Q.; Zachman, M. J.; Kabir, S.; Liang, J.; Zhu, J.; Slenker, B.; Pupucevski, M.; Macauley, N.; Kropf, A. J.; Zeng, H.; Strasser, D.; Myers, D. J.; Xu, H.; Zeng, Z.; Yan, Y.; Wu, G. Regulating the Third Metal to Design and Engineer Multilayered NiFeM (M: Co, Mn, and Cu) Nanofoam Anode Catalysts for Anion-

- Exchange Membrane Water Electrolyzers. *Adv. Energy Mater.* **2024**, *14* (26), 2400029.
- (19) Shi, G.; Tano, T.; Tryk, D. A.; Yamaguchi, M.; Iiyama, A.; Uchida, M.; Iida, K.; Arata, C.; Watanabe, S.; Kakinuma, K. Temperature Dependence of Oxygen Evolution Reaction Activity in Alkaline Solution at Ni–Co Oxide Catalysts with Amorphous/Crystalline Surfaces. *ACS Catal.* **2022**, *12* (22), 14209–14219.
- (20) Shi, G.; Arata, C.; Tryk, D. A.; Tano, T.; Yamaguchi, M.; Iiyama, A.; Uchida, M.; Iida, K.; Watanabe, S.; Kakinuma, K. NiFe Alloy Integrated with Amorphous/Crystalline NiFe Oxide as an Electrocatalyst for Alkaline Hydrogen and Oxygen Evolution Reactions. *ACS Omega* **2023**, *8* (14), 13068–13077.
- (21) Shi, G.; Tano, T.; Iwataki, T.; Tryk, D. A.; Uchida, M.; Iiyama, A.; Terao, K.; Tamoto, K.; Yamaguchi, M.; Miyatake, K.; Kakinuma, K. Highly Active Nanostructured NiCoMo-Based Catalyst for Oxygen Evolution in Anion-Exchange Membrane Water Electrolysis. *ACS Appl. Energy Mater.* **2023**, *6* (21), 10742–10747.
- (22) Mitsushima, S.; Ioroi, T.; Kuroda, Y.; Nagasawa, K.; Uchiyama, T.; Orikasa, Y.; Inoue, H.; Higuchi, E.; Ando, K.; Nakajima, T.; Misumi, R.; Uchimoto, Y. Electrochemical Methods for Water Electrolysis Electrodes and Electrocatalysts. *Denki Kagaku* **2022**, *90* (2), 136–158.
- (23) Ono, H.; Kimura, T.; Takano, A.; Asazawa, K.; Miyake, J.; Inukai, J.; Miyatake, K. Robust Anion Conductive Polymers Containing Perfluoroalkylene and Pendant Ammonium Groups for High Performance Fuel Cells. *J. Mater. Chem. A* **2017**, *5* (47), 24804–24812.
- (24) Nagasawa, K.; Ishida, T.; Kashiwagi, H.; Sano, Y.; Mitsushima, S. Design and Characterization of Compact Proton Exchange Membrane Water Electrolyzer for Component Evaluation Test. *Int. J. Hydrogen Energy* **2021**, *46* (74), 36619–36628.
- (25) Luo, Y.; Zhang, Z.; Chhowalla, M.; Liu, B. Recent Advances in Design of Electrocatalysts for High-Current-Density Water Splitting. *Adv. Mater.* **2022**, *34* (16), 2108133.
- (26) Ozawa, Y.; Iwataki, T.; Uchida, M.; Kakinuma, K.; Miyatake, K. The Effect of the Piperidinium Structure on Anion-Exchange Membranes for Applications in Alkaline Water Electrolysis Cells. *J. Mater. Chem. A* **2023**, *11* (37), 19925–19935.
- (27) Liu, F.; Miyatake, K.; Tanabe, M.; Mahmoud, A. M. A.; Yadav, V.; Guo, L.; Wong, C. Y.; Xian, F.; Iwataki, T.; Uchida, M.; Kakinuma, K. High-Performance Anion Exchange Membrane Water Electrolyzers Enabled by Highly Gas Permeable and Dimensionally Stable Anion Exchange Ionomers. *Adv. Sci.* **2024**, *11* (29), 2402969.
- (28) Yadav, V.; Miyatake, K.; Mahmoud, A. M. A.; Liu, F.; Xian, F.; Guo, L.; Wong, C. Y.; Iwataki, T.; Uchida, M.; Kakinuma, K. Poly(Arylene Piperidinium) Terpolymer Membranes with Dual Piperidinium Cations and Semi-Fluoroalkyl Pendants for Anion Exchange Membrane Water Electrolyzers. *J. Mater. Chem. A* **2024**, *12* (37), 25429–25441.
- (29) Liu, F.; Miyatake, K.; Mahmoud, A. M. A.; Yadav, V.; Xian, F.; Guo, L.; Wong, C. Y.; Iwataki, T.; Shirase, Y.; Kakinuma, K.; Uchida, M. Polyphenylene-Based Anion Exchange Membranes with Robust Hydrophobic Components Designed for High-Performance and Durable Anion Exchange Membrane Water Electrolyzers Using Non-PGM Anode Catalysts. *Adv. Energy Mater.* **2024**, 2404089.
- (30) McCrory, C. C. L.; Jung, S.; Peters, J. C.; Jaramillo, T. F. Benchmarking Heterogeneous Electrocatalysts for the Oxygen Evolution Reaction. *J. Am. Chem. Soc.* **2013**, *135* (45), 16977–16987.
- (31) Wang, Z.; Guo, X.; Montoya, J.; Nørskov, J. K. Predicting Aqueous Stability of Solid with Computed Pourbaix Diagram Using SCAN Functional. *npj Comput. Mater.* **2020**, *6* (1), 160.
- (32) Huang, L.-F.; Hutchison, M. J.; Santucci, R. J., Jr.; Scully, J. R.; Rondinelli, J. M. Improved Electrochemical Phase Diagrams from Theory and Experiment: The Ni–Water System and Its Complex Compounds. *J. Phys. Chem. C* **2017**, *121* (18), 9782–9789.
- (33) Chung, D. Y.; Lopes, P. P.; Martins, P. F. B. D.; He, H.; Kawaguchi, T.; Zapol, P.; You, H.; Tripkovic, D.; Strmcnik, D.; Zhu, Y.; Seifert, S.; Lee, S.; Stamenkovic, V. R.; Markovic, N. M. Dynamic Stability of Active Sites in Hydr(Oxy)Oxides for the Oxygen Evolution Reaction. *Nat. Energy* **2020**, *5* (3), 222–230.
- (34) Li, Y.-K.; Zhang, G.; Lu, W.-T.; Cao, F.-F. Amorphous Ni–Fe–Mo Suboxides Coupled with Ni Network as Porous Nanoplate Array on Nickel Foam: A Highly Efficient and Durable Bifunctional Electrode for Overall Water Splitting. *Adv. Sci.* **2020**, *7* (7), 1902034.
- (35) Saji, V. S.; Lee, C.-W. Molybdenum, Molybdenum Oxides, and Their Electrochemistry. *ChemSusChem* **2012**, *5* (7), 1146–1161.
- (36) Ke, J.; Zhang, J.; Zhang, L.; He, S.; Zhong, C.; Du, L.; Song, H.; Fang, X.; Zhang, Z.; Cui, Z. Role of High-Valence Metal Dissolution in Oxygen Evolution Kinetics of the Advanced FeNiO_x Catalysts. *ACS Catal.* **2024**, *14* (21), 16363–16373.
- (37) Song, W.; Xia, C.; Zaman, S.; Chen, S.; Xiao, C. Advances in Stability of NiFe-Based Anodes toward Oxygen Evolution Reaction for Alkaline Water Electrolysis. *Small* **2024**, *20* (48), 2406075.

CAS INSIGHTS™
EXPLORE THE INNOVATIONS SHAPING TOMORROW

Discover the latest scientific research and trends with CAS Insights. Subscribe for email updates on new articles, reports, and webinars at the intersection of science and innovation.

[Subscribe today](#)

CAS
A division of the American Chemical Society